On the Accuracy of Numerical Wave Making Techniques

by Jong-Chun Park*, *Member* Ming Zhu**, *Member*
Hideaki Miyata**, *Member*

Summary

Two numerical wave making techniques are examined with respect to the degree of accuracy. One technique is for the finite-volume method in the curvilinear, boundary-fitted coordinate system and the other is for the finite-difference method in a rectangular coordinate system. The free-surface treatments of the latter are for a two-layer flow and can cope with 3D wave breaking. The wave making techniques are explained and the accuracy and improvement of the techniques are described by the comparison with the records of physically generated waves.

1. Introduction

Since a remarkable part of fluid flow is under the presence of free-surface, the numerical simulation of free-surface motions is of significant importance for both scientific and engineering purposes. Following the original MAC method some numerical techniques for the solution of the Navier-Stokes equation have been developed in the framework of an inflexible, rectangular grid system at the authors' laboratory since 1979. They are called Tokyo University Modified Marker-And-Cell (TUMMAC) method. Almost all versions, both 2D and 3D, are for the flows with free-surfaces. The TUMMAC-IV method for ship waves[1] and the TUMMAC-V method for 2D breaking waves[2] are typical examples among numerous versions.

The free-surface conditions in those works are common to the original MAC method and its modification. The viscous stresses and surface tension are ignored and then the dynamic condition is fulfilled by the pressure condition on the free-surface while the kinematic condition is by the Lagrangian movement of markers or segments. The accuracy of these techniques has been well demonstrated for the problems of gravitational waves.

In this paper two other numerical simulation techniques are dealt with and their properties in the simulation of the free-surface motions are examined. Since the numerical wave making technique plays an important role for the establishment of a numerical basin, the stress is not only on the free-surface treatments but also on the wave making treatments at the inflow boundary.

The aim of this paper is to develop two techniques, one is a finite-volume method called WISDAM-V which employs a curvilinear coordinate system fitted both to the body surface and to the free-surface[5][6]. A quite similar approach was previously pursued by a finite-difference method[3][4] and some successful results were obtained at relatively low Reynolds numbers. The robustness is improved by the employment of the finite-volume discretization in the WISDAM-V method.

The second is a finite-difference method for a two-layer flow in the framework of a rectangular coordinate system. It is called TUMMAC-VI method which has first succeeded in 3D breaking wave simulation[7]. Contrary to other TUMMAC methods the very special treatments are devised in this study, however, its accuracy in the wave formation is not yet fully verified.

In this paper regular periodic waves are generated by these two numerical techniques and the accuracy of the generated waves are compared with the rocords of physically generated waves by a flap-type wave generator. The viscous stresses on the free-surface are very grossly treated or ignored and the surface tension is not considered since their effect are almost negligible in the problems described herewith.

2. WISDAM-V Finite-Volume Method

2.1 Computational procedure

The computational procedure is similar to the previous studies[5][6] with the incorporation of the effect of moving coordinate system into the governing equations. The velocities and pressure points are defined in a

* Graduate School, Dept. Naval Architecture and Ocean Engineering, University of Tokyo
** Dept. Naval Architecture and Ocean Engineering, University of Tokyo

Received 11th Jan 1993
Read at the Spring meeting 19, 20th May 1993

staggered manner in the curvilinear coordinate system. The Cartesian coordinates are chosen as the basic coordinate system of the physical region, and the governing equations are formulated by a so-called "partial transformation" technique. Suppose that the position vector of the coordinate system is

$$\boldsymbol{r}=\boldsymbol{r}(x^1, x^2, x^3), \tag{1}$$

where x^1, x^2, x^3 are longitudinal, lateral and vertical coordinates, respectively, then the transformation of coordinate system between the physical region and the transformed region is

$$\mathbf{grad}\ \xi^r=\left(\frac{\partial \boldsymbol{r}}{\partial \xi^1}, \frac{\partial \boldsymbol{r}}{\partial \xi^2}, \frac{\partial \boldsymbol{r}}{\partial \xi^3}\right)^T. \tag{2}$$

Hence the determination of the above matrix, or the so-called Jacobian, which corresponds to the local volume about its definition point, becomes,

$$J=\det(\mathbf{grad}\ \xi^r). \tag{3}$$

Then the element of the inverse transformation matrix of Eq. (2) is

$$\frac{\partial \xi^l}{\partial x^p}=\frac{1}{J}\left[\frac{\partial x^s}{\partial \xi^m}\frac{\partial x^t}{\partial \xi^n}-\frac{\partial x^t}{\partial \xi^m}\frac{\partial x^s}{\partial \xi^n}\right], \tag{4}$$

with (l, m, n) and (p, s, t) in a cyclic order. In the present study, in order to employ a finite-volume approach for formulating the governing equation, the so-called "area vector" is adopted instead of Eq. (4).

$$S_p^l=J\frac{\partial \xi^l}{\partial x^p}=\left[\frac{\partial x^s}{\partial \xi^m}\frac{\partial x^t}{\partial \xi^n}-\frac{\partial x^t}{\partial \xi^m}\frac{\partial x^s}{\partial \xi^n}\right], \tag{5}$$

where the superscript of the area vector expresses its respective contravariant direction, while the subscript means its Cartesian components, i. e., an area vector is defined for the respective contravariant direction, and its value is the area of the surface (of the local volume) normal to its direction. Thus the vector form for $\boldsymbol{S}^m$ in the Cartesian coordinates is,

$$\boldsymbol{S}^m=(S_1^m, S_2^m, S_3^m). \tag{6}$$

Thus, the Jacobian J and the area vector $\boldsymbol{S}^m$ are defined as the geometric coefficients in the present study.

For the incompressible viscous flow, the Navier-Stokes equation can be written into the following conservative form in a moving coordinate system.

$$\frac{1}{J}\frac{\partial(J\boldsymbol{u})}{\partial t}+\mathrm{div}\ \boldsymbol{T}=\boldsymbol{F}, \tag{7}$$

here, $\boldsymbol{F}$ is the external force, $\boldsymbol{u}$ is the velocity, and the stress tensor $\boldsymbol{T}$ is defined as

$$\boldsymbol{T}=p\bar{I}+(\boldsymbol{u}-\boldsymbol{v})\boldsymbol{u}-\nu\ \mathbf{def}\ \boldsymbol{u}, \tag{8}$$

where $\bar{I}$ is the unit tensor, $\boldsymbol{v}$ is the moving velocity of grid point, ν is the kinematic molecular viscosity of the fluid, p is the pressure divided by the fluid density and the fluid deformation is defined as,

$$\mathbf{def}\ \boldsymbol{u}=\mathbf{grad}\ \boldsymbol{u}+(\mathbf{grad}\ \boldsymbol{u})^T. \tag{9}$$

Therefore the stress tensor $\boldsymbol{T}$ in Eq. (8) is composed of the normal stress of pressure, nonlinear stress, viscous stresses.

Assuming that the external force is the gravitational force, Eq. (7) becomes,

$$\frac{1}{J}\frac{\partial(J\boldsymbol{u})}{\partial t}=-\mathbf{grad}\ H+\boldsymbol{f}, \tag{10}$$

and

$$\boldsymbol{f}=\mathrm{div}\ \bar{\tau}, \tag{11}$$

then,

$$\bar{\tau}=-(\boldsymbol{u}-\boldsymbol{v})\boldsymbol{u}+\nu\ \mathbf{def}\ \boldsymbol{u}, \tag{12}$$

$$H=p+gx^3, \tag{13}$$

where g is gravitational acceleration. Therefore in the present study, H is solved instead of the pressure p.

The continuity equation for the incompressible flow is as follows.

$$\mathrm{div}(\boldsymbol{u})=0. \tag{14}$$

The MAC-type algorithm is used for the solution procedure. The velocity is updated by an explicit time-marching method in the present study. Suppose that the flow field is determined in the (n)-th time step, the free surface boundary is deformed according to its kinematic condition which will be described in the following section. Then the grid is regenerated so as to fit the deformed free-surface boundary. The pressure is solved in the new free-surface-fitted coordinate system. The details of the solution procedure is described in Ref. [5][6] and they are abbreviated here.

2.2 Free-surface condition

Suppose that the deformed free-surface is given as ξ^3 =const. in the curvilinear boundary-fitted coordinate system. In the present study, the nonlinear kinematic condition and the inviscid dynamic condition are imposed on this surface. The nonlinear kinematic condition is written as follows.

$$\frac{\partial F}{\partial t}+u^i\frac{\partial F}{\partial x^i}=0, \tag{15}$$

where F is a function to represent the free-surface. Therefore, the nonlinear kinematic condition is used to be employed for the determination of free-surface position in the numerical calculation. In the previous studies for the ship wave problems[3)4)5)6)], F is defined by the wave height function so that the nonlinear kinematic condition can be written as,

$$\frac{\partial x^3}{\partial t}+u^1\frac{\partial x^3}{\partial x^1}+u^2\frac{\partial x^3}{\partial x^2}-u^3=0, \tag{16}$$

when x^3 is the Cartesian coordinate to present the free-surface. However, as shown in the works by Yamazaki[10)] and Hinatsu[11)], in the curvilinear coordinate system it will be more reasonable to employ ξ^3= const. as F. Therefore, Eq. (15) becomes,

$$\frac{\partial \xi^3}{\partial t}+u^i\frac{\partial \xi^3}{\partial x^i}=0. \tag{17}$$

Therefore the nonlinear kinematic condition used in the present study is the inverse form of the above equation as follows.

$$\frac{\partial x^i}{\partial t}-JU^3\frac{S_j^3\delta^{ij}}{\|S^3\|^2}=0, \tag{18}$$

where U^3 is the contravariant velocity at the free-surface. This equation means that the free-surface is deformed so as to preserve the mass at the free-surface. In the present study, only the wave height x^3 is updated in an Euler manner by using Eq. (18)[12)].

Since the viscous stress is ignored in this study, the dynamic condition on the free-surface is

$$H=gx^3. \tag{19}$$

2.3 Wave making condition

The computational region is a three-dimensional rectangular region with a numerical wave maker set at the inflow boundary. The wave is generated in a manner based on the linear wave theory. As shown in Fig. 1, the inflow velocities are given as follows.

$$u^1=a\sigma\frac{\cosh(x\{D+x^3\})}{\sinh(xD)}\sin(\sigma t-x\cdot r) \quad \text{at } x^1=0,\ 1, \tag{20 a}$$

$$u^2=0.0 \quad \text{at } \xi^1=0,\ 1, \tag{20 b}$$

$$u^3=a\sigma\frac{\sinh(x\{D+x^3\})}{\sinh(xD)}\cos(\sigma t-x\cdot r) \quad \text{at } x^1=0,\ 1,\ 2, \tag{20 c}$$

where a is the half wave height, σ is the angular frequency, x is the wave number and D is the depth of the region. r is the position vector of the definition points and x^3 is their coordinate in the x^3-direction when the still water surface is set at $x^3=0.0$. The wave height at the inflow boundary is set as follows.

$$x^3=a\sin(\sigma t-x\cdot r), \text{ at } \xi^1=0,\ 1. \tag{21}$$

2.4 Boundary conditions

A cyclic boundary condition is imposed at the lateral boundary of the three-dimensional computational region. At the bottom boundary, the velocity is given to have no normal gradient and the pressure is set at the hydrostatic value since the bottom boundary is located deep enough in comparison with the wave length considered.

In the free-surface wave problem, the open boundary condition is important. There are several methods such as the Sommerfeld-Orlanski condition, its modifications[13)14)], the added dissipation zone method[15)] and its combination with the artificial damping scheme[11)16)17)]. In the present study, the added dissipation zone method with the artificial damping scheme is employed as the wave absorbing condition. An artificial damping scheme in the dissipation zone is added to the right-hand-side of Eq. (10) as follows.

$$\boldsymbol{a}=\left(0.0,\ 0.0,\ -0.5\left(\frac{\xi^1-\xi^1_{ds}}{\xi^1_{de}-\xi^1_{ds}}\right)^2\left(\frac{\xi^3-\xi^3_{bt}}{\xi^3_{fs}-\xi^3_{bt}}\right)\right)\cdot\boldsymbol{u}$$

$$\xi^1_{ds}<\xi^1<\xi^1_{de},\ \xi^3_{bt}<\xi^3<\xi^3_{fs}, \tag{22}$$

where ξ^1, ξ^3 are the transformed coordinates, and the subscripts ds and de denote the coordinates of the start and end points of the added dissipation zone in the ξ^1-direction. bt denotes the bottom and fs the free-surface position of the zone in the ξ^3-direction.

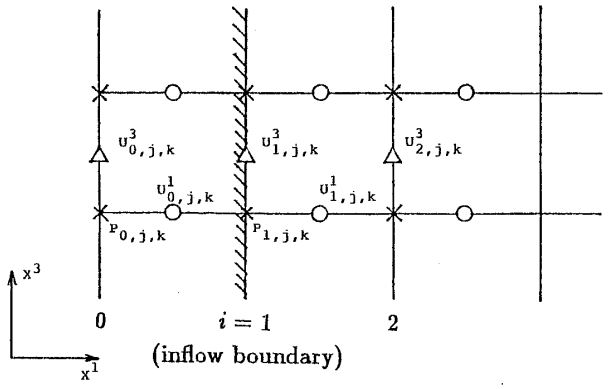

Fig. 1 Definition sketch for the wave making condition (case A).

3. Simulated Waves by WISDAM-V Method

3.1 Condition of computation

Regular waves with small amplitude are generated and the degree of accuracy is examined with the physically measured wave records at the experimental tank. The condition of computation is listed in Table 1. The conditions of the two methods, i.e., WISDAM-V (case A) and TUMMAC-VI (case B), were kept the same as far as possible.

Three wave periods of 0.9, 1.2 and 1.5 second are chosen with the constant wave height of 0.06 m. Since the wave length is greater than 21 times of wave height, the nonlinearity of waves is supposed to be very small.

The grids are attracted in the vicinity of the free-surface as shown in Fig. 2 so that satisfactory resolution can be obtained with a limited number of grid points. The horizontal spacing is set at 4 percent of wave length. Therefore the computational domain is stretched due to the elongation of the wave length. For the added dissipation zone of wave absorption 20 horizontal grid points are allotted and the horizontal spacing is stretched exponentially as shown in Fig. 2.

Table 1 Condition of compuation.

	Case A	Case B
Simulation Code	WISDAM-V	TUMMAC-VI
Computational domain		
length (m)	4λ	3λ
width (m)	0.5	-
depth (m)	3.0	2.5
Number of grid points		
horizontal	101	171
vertical	31	145
lateral	5	-
Grid spacing		
horizontal (m)	0.04λ	0.02λ
vertical (m)	$5*10^{-4}$ (min)	$3*10^{-3}$ (min)
lateral (m)	0.1	-
kinematic viscosity (m^2/s)	$1.0107*10^{-6}$ (fresh water)	
Wave		
period T (sec)	0.9,1.2,1.5	
length λ (m)	1.260, 2.246, 3.51	
height $2a$ (m)	0.06	

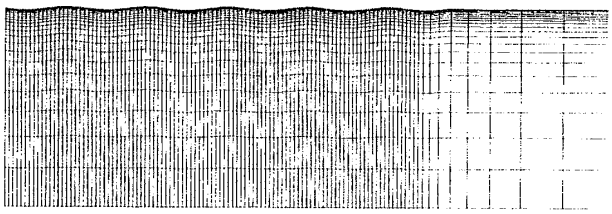

Fig. 2 Boundary-fitted grid system.

The physically measured wave records were presented from the Seakeeping Tank of the University of Tokyo which is 45 m long, 5 m wide and 3.5 m deep. Regular waves were generated by a flap-type wave generator and their profiles were recorded by a wave probe of capacitance type. The wave records were instantaneously digitized and stored in a personal computer. In order to compare with the computation, a low-pass filter is employed to eliminate the mechanical noise at high frequencies (higher than 500 frequency) in the wave profile records. The difference of the wave profile due to the change of the stroke of wave maker is shown in Fig. 3. It is very hard to have wave height with exact accordance with the predetermined value. The error of experiment is noted in this figure.

3.2 Results

An example of velocity vector field is shown in Fig. 4. It is noted that the damping of velocity field by the added dissipation zone is well performed.

Comparison of wave profiles in time and space is made in Figs. 5 and 6, and that of wave spectra in Figs. 7 and 8. In these figures X denotes longitudinal coordinate in meter. T is the wave period and the frequency is defined as

$$\text{frequency}=\frac{2\pi}{T} \tag{23}$$

It is obviously noted that the time-variation of wave profile is small, which implies that the contamination by the numerical error is negligibly small. Considering that some errors are also inevitable in the measurement as shown in Fig. 3, the agreement between numerical simulation and experiment is good. It is realized in the simulation that the slope of the wave profile is gentle on the trough, while it is steeper on the crests, especially when the wave height to length ratio is larger.

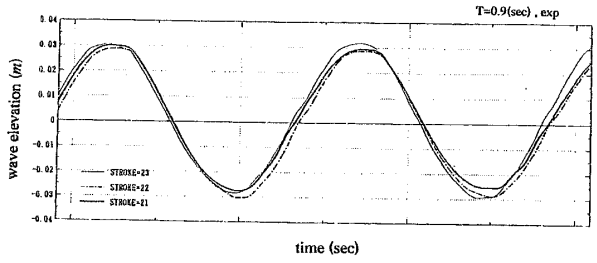

Fig. 3 Variation of physically generated wave profile due to the difference of the stroke of wavemaker

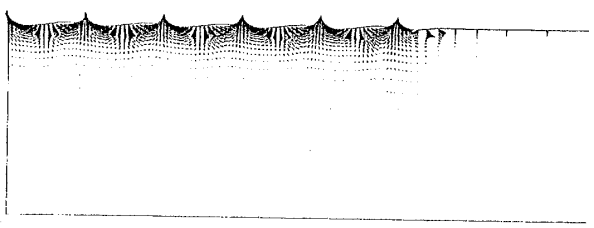

Fig. 4 Velocity vector field of the case A.

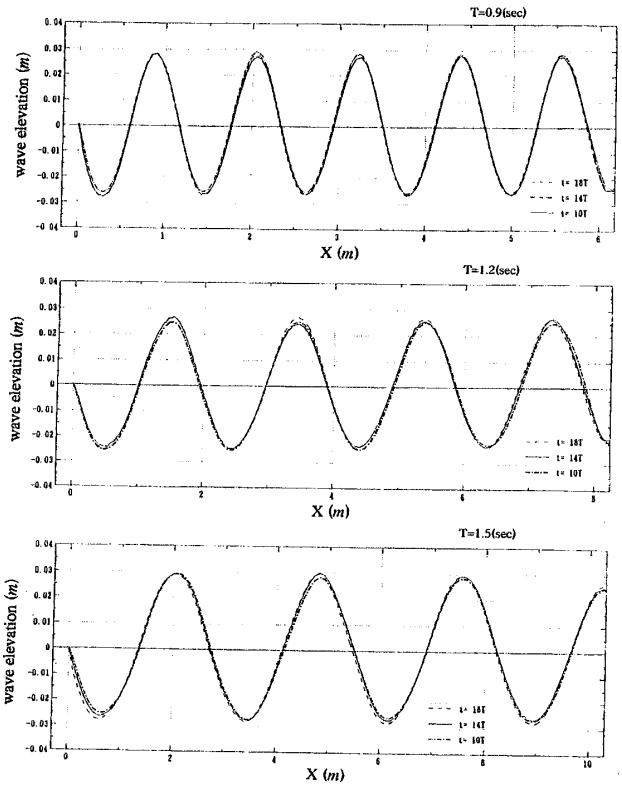

Fig. 5 Time variation of the wave profile (case A).

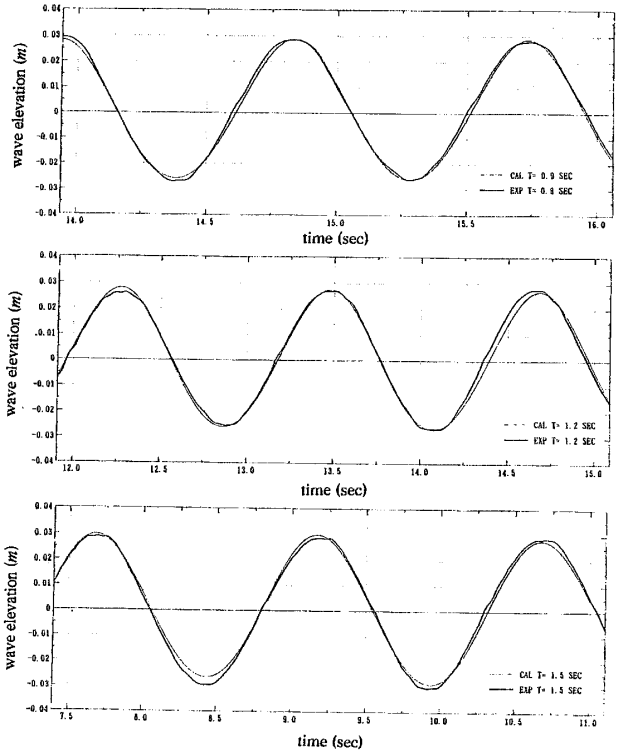

Fig. 6 Comparison of wave profile with measured records (case A).

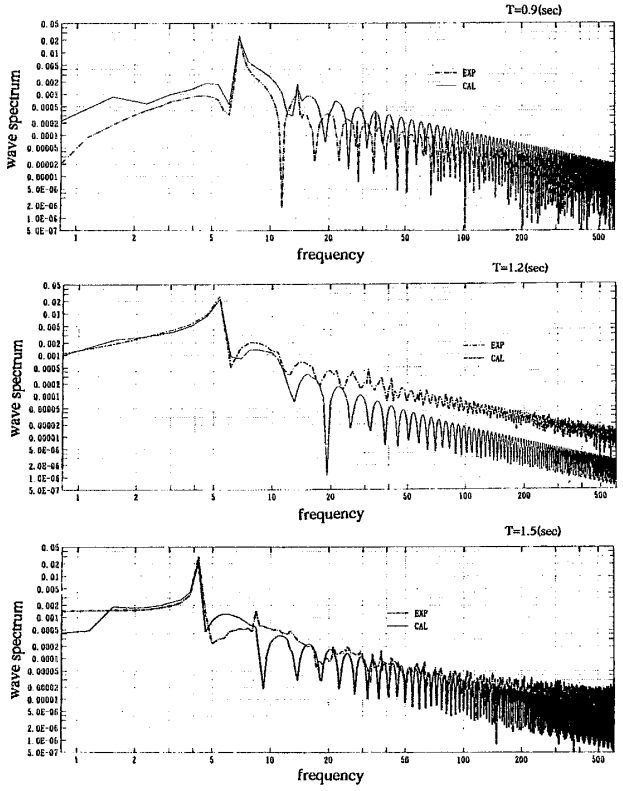

Fig. 7 Comparison of logarithmic wave spectrum (case A).

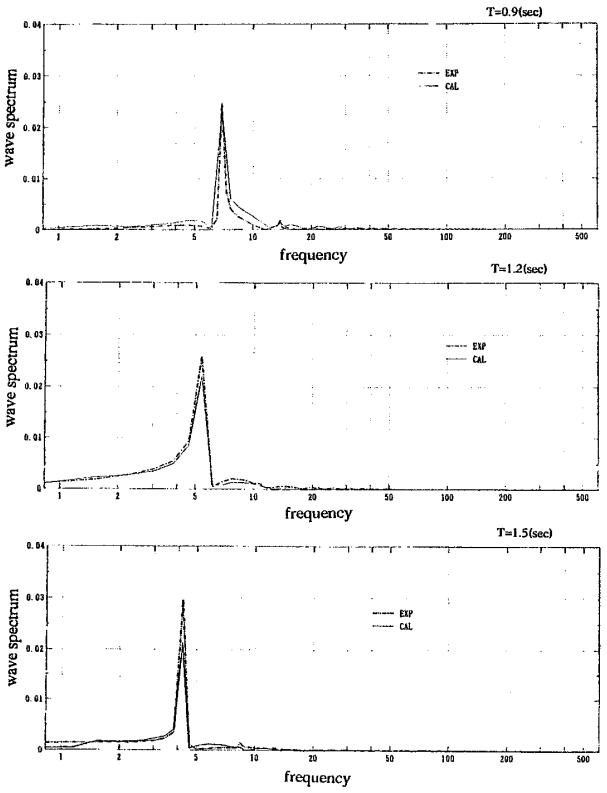

Fig. 8 Comparison of wave spectrum (case A).

4. TUMMAC-VI Finite-Difference Method

4.1 Computational procedure

The TUMMAC-VI method[7] which first succeeded in the simulations of 3D wave breaking and water-sand flow is used here.

Assuming that the fluid flows in the two-layer with the specific density are incompressible and continuous, the governing equations for the two-layer flow are the following continuity and Navier-Stokes equations for the two fluids, respectively.

$$\rho^{<1>}(\nabla\cdot\boldsymbol{u})=0, \tag{24 a}$$

$$\rho^{<2>}(\nabla\cdot\boldsymbol{u})=0, \tag{24 b}$$

$$\frac{\partial\boldsymbol{u}}{\partial t}+(\boldsymbol{u}\cdot\nabla)\boldsymbol{u}=-\frac{1}{\rho^{<1>}}\nabla p+\boldsymbol{a}^{<1>}, \tag{25 a}$$

$$\frac{\partial\boldsymbol{u}}{\partial t}+(\boldsymbol{u}\cdot\nabla)\boldsymbol{u}=-\frac{1}{\rho^{<2>}}\nabla p+\boldsymbol{a}^{<2>}, \tag{25 b}$$

where,

$$\boldsymbol{a}=\nu\nabla^2\boldsymbol{u}+\boldsymbol{f}, \tag{26}$$

here, the superscripts $\langle 1\rangle$ and $\langle 2\rangle$ denote the fluid below and above the interface, respectively, in the present study $\langle 1\rangle$ correspond to the water region below and $\langle 2\rangle$ the air region on it, ∇ is the gradient operator, $\boldsymbol{u}$, p, t and ν are the velocity, the pressure, the time and the kinematic viscosity, respectively, and $\boldsymbol{f}$ is the external force including the gravitational acceleration.

The substantial concept and computational procedure of the TUMMAC-VI are described in Ref. [7], and they are only very briefly described here.

The fluid region is assumed to be divided into the upper and lower layers and the solution of the above governing equations is performed quite separately at each time step of time-marching. The configuration of the interface is determined by the free-surface condition described in the subsequent section and both the velocity and the pressure are assumed to be continuous at the interface. The surface tension is not considered here.

The solution algorithm for each layer is similar to the previous TUMMAC method[1)2)8)] in which the velocity and pressure points are defined in a staggered manner in a rectangular coordinate system.

4.2 Free-surface condition

Since the viscous stresses are ignored at the free-surface the following dynamic and kinematic conditions are considered.

$$p^{<1>}=p^{<2>}, \tag{27}$$

$$\frac{\partial f}{\partial t}+u\frac{\partial f}{\partial x}+v\frac{\partial f}{\partial y}+w\frac{\partial f}{\partial z}=0. \tag{28}$$

Here, f denotes the free-surface location, and u, v, w the velocities in the respective x, y, z directions, contrary to the case A, the x, y, z represent the longitudinal, lateral and vertical coordinates. Eq. (28) means that the particle on the free-surface stays there by the free-surface movement, and does not seem to be appropriate for the strongly interacting free-surface motions which include overturning and breaking behaviors.

For the movement of fluid interface the following equation of the marker-density is introduced.

$$\frac{\partial M_\rho}{\partial t}+u\frac{\partial M_\rho}{\partial x}+v\frac{\partial M_\rho}{\partial y}+w\frac{\partial M_\rho}{\partial z}=0. \tag{29}$$

Here, the marker-density M_ρ is assumed to take the value between $\rho^{<1>}$ and $\rho^{<2>}$ all over the computational domain and this scalar value has the meaning of porosity in each cell. In the case that an air-water flow is considered the value of M_ρ means the volume fraction of water in a cell.

Eq. (29) is calculated at each time step and the free-surface location is determined to be a point where the marker-density takes the mean value of $\rho^{<1>}$ and $\rho^{<2>}$ as

$$M_\rho=\tilde{M}_\rho=\frac{(\rho^{<1>}+\rho^{<2>})}{2}. \tag{30}$$

After determining the free-surface location the two fluid regions are treated separately and the Navier-Sokes equation is integrated with the respective density $\rho^{<1>}$ and $\rho^{<2>}$. The free-surface location and pressure on this surface are used as boundary conditions in this process.

The dynamic free-surface condition of Eq. (27) is implemented by the so-called "irregular star" technique[18] in the solution process of the Poisson equation for the pressure. The length of leg in the irregular star technique is calculated using the marker-density as for the positive x-direction.

$$\eta=\frac{M_{\rho i}-\tilde{M}_\rho}{M_{\rho i}-M_{\rho i+1}}\cdot\Delta_i, \tag{31}$$

where, Δ is the spacing and the subscript i is used for the x location.

In the present problem, it is very important to extrapolate the physical values into the other layer, since the fluid motion at the interface is determined by the interaction between the fluids of two-layers. Therefore, the pressure at the interface is determined by extrapolating the pressure of the fluid 〈2〉 to the interface location. The pressure is extrapolated with zero gradient in the horizontal and lateral direction while the static pressure difference due to the gravitation is considered in the vertical direction.

At the interface the velocities are extrapolated with approximately no normal gradient from the fluid 〈1〉 to the fluid 〈2〉. The velocities are horizontally extrapolated when the interface slope is greater than 45° or vertically otherwise. This treatment very grossly corresponds with the viscous tangential condition at the free-surface.

4.3 Difference equation for the marker-density

For the finite-difference approximation of the marker-density equation (29), the Adams-Bashforth method is used for time-differencing as follows.

$$M_\rho^{(n+1)}=M_\rho^{(n)}-\Delta t\left[\frac{3\hat{M}^{(n)}-\hat{M}^{(n-1)}}{2}\right], \tag{32}$$

where,

$$\hat{M}=u\frac{\partial M_\rho}{\partial x}+v\frac{\partial M_\rho}{\partial y}+w\frac{\partial M_\rho}{\partial z}. \tag{33}$$

The preliminary test computations proved that the use of the Adams-Bashforth method is very effective for the prevention of the excessive diffusion of the marker-density.

For the space differencing terms of Eq. (29), a variety of scheme are tested. The scheme representation is as follows for the first term for simplicity.

(1) the 1st-order upwind differencing

$$\hat{M}_i=u_0\frac{M_{\rho i}-M_{\rho i-1}}{\Delta_{i-1/2}}(\text{if } u_0\geq 0),$$
$$=u_0\frac{M_{\rho i+1}-M_{\rho i}}{\Delta_{i+1/2}}(\text{if } u_0<0), \tag{34}$$

where,

$$u_0=\frac{u_{i-1/2}+u_{i+1/2}}{2}. \tag{35}$$

(2) the 2nd-order centered differencing

$$\hat{M}_i=u_0\frac{M_{\rho i+1}-M_{\rho i-1}}{\Delta_i}. \tag{36}$$

(3) the 2nd-order centered differencing+filter

Here, the filter is used only in the vertical direction as follows.

$$\frac{-M_{\rho i+2}-4M_{\rho i+1}+10M_{\rho i}+4M_{\rho i-1}-M_{\rho i-2}}{16}. \tag{37}$$

(4) the 2nd-order compact scheme

The compact differencing method by Hirsh[19] is used here as

$$\frac{(\hat{M}_{i+1}+4\hat{M}_i+\hat{M}_{i-1})}{6}=u_0\frac{(M_{\rho i+1}-M_{\rho i-1})}{2\Delta_i}. \tag{38}$$

The differential coefficient $\hat{M}_i$ is simultaneously calculated along a coordinate line by the numerical solution of the triagonal linear system. However, for the computational efficiency the initial value of $\hat{M}_i$ is predicted by the centered differencing as

$$\hat{M}_i^{(0)}=u_0\frac{M_{\rho i+1}-M_{\rho i-1}}{2\Delta_i}, \tag{39}$$

and then an iterative calculation is made to raise the accuracy up to the fourth-order through the following equations derived from Eq. (38)[20].

$$\hat{M}_i^{(m+1)}=\hat{M}_i^{(m)}+\bar{\omega}\left\{-\frac{(\hat{M}_{i+1}+4\hat{M}_i+\hat{M}_{i-1})}{6}+u_0\frac{(M_{\rho i+1}-M_{\rho i-1})}{2\Delta_i}\right\}^{(m)} \tag{40}$$

where the relaxation factor $\bar{\omega}$ is set at 0.6.

(5) the 2nd-order compact differencing+filter

(6) the 3rd-order upwind differencing

It is attained in the upwind differencing manner as follows

$$\hat{M}_i=u_0\frac{M_{\rho i+1/2}-M_{\rho i-1/2}}{\Delta_i}, \tag{41}$$

where,

$$M_{\rho i+1/2}=M^L_{\rho i+1/2}(\text{if } u_{i+1/2}\geq 0)$$
$$=M^R_{\rho i+1/2}(\text{if } u_{i+1/2}<0). \tag{42}$$

In the case of the variable mesh system, the value of $M^L_{\rho i+1/2}$ and $M^R_{\rho i+1/2}$ are determined following Ref. [21] [22], as

$$M^L_{\rho i+1/2}=M_{\rho i}+\Delta_{L1}(M_{\rho i}-M_{\rho i-1})+\Delta_{L2}(M_{\rho i+1}-M_{\rho i}), \tag{43 a}$$

$$M^R_{\rho i+1/2}=M_{\rho i}+(1-\Delta_{R1})(M_{\rho i+1}-M_{\rho i})-\Delta_{R2}(M_{\rho i+2}-M_{\rho i+1}), \tag{43 b}$$

where,

$$\Delta_{L1}=\frac{\Delta_i\Delta_{i+1}}{(\Delta_{i-1}+\Delta_i+\Delta_{i+1})(\Delta_{i-1}+\Delta_i)},$$

$$\Delta_{L2}=\frac{\Delta_i(\Delta_{i-1}+\Delta_i)}{(\Delta_{i-1}+\Delta_i+\Delta_{i+1})(\Delta_i+\Delta_{i+1})},$$

$$\Delta_{R1}=\frac{\Delta_{i+1}(\Delta_{i+1}+\Delta_{i+2})}{(\Delta_i+\Delta_{i+1}+\Delta_{i+2})(\Delta_i+\Delta_{i+1})},$$

$$\Delta_{R2}=\frac{\Delta_i\Delta_{i+1}}{(\Delta_i+\Delta_{i+1}+\Delta_{i+2})(\Delta_{i+1}+\Delta_{i+2})}.$$

Since the value of the marker-density is numerically diffused across the interface in the course of the computation of Eq. (29) at each time step, the present method obscures the interface location and the accuracy is inferior to the other methods unless an appropriate scheme is employed and very fine grid spacing and time increment are used.

4.4 Wave making condition

In this problem of numerical wave making, we suppose the layer ⟨1⟩ and ⟨2⟩ to be water and air, respectively.

The computational region is a two-dimensional rectangular region with a numerical wave maker set at the inflow boundary of the region ⟨1⟩. Since the wave in the region ⟨1⟩ is generated in a manner based on the linear theory of a finite-amplitude wave, the inflow velocities in the region ⟨1⟩ defined in Fig. 9 are given as follows.

$$u_1=a\sigma\frac{\cosh\{x(D+z)\}}{\sinh(xD)}\sin(\sigma t-xx), \tag{44 a}$$

$$u_2=a\sigma\frac{\cosh\{x(D+z)\}}{\sinh(xD)}\sin\{\sigma t-x(x-\Delta x)\}, \tag{44 b}$$

$$w_1=a\sigma\frac{\sinh\left\{x\left(D+z+\frac{\Delta z}{2}\right)\right\}}{\sinh(xD)}\cos\left\{\sigma t-x\left(x-\frac{\Delta x}{2}\right)\right\}, \tag{44 c}$$

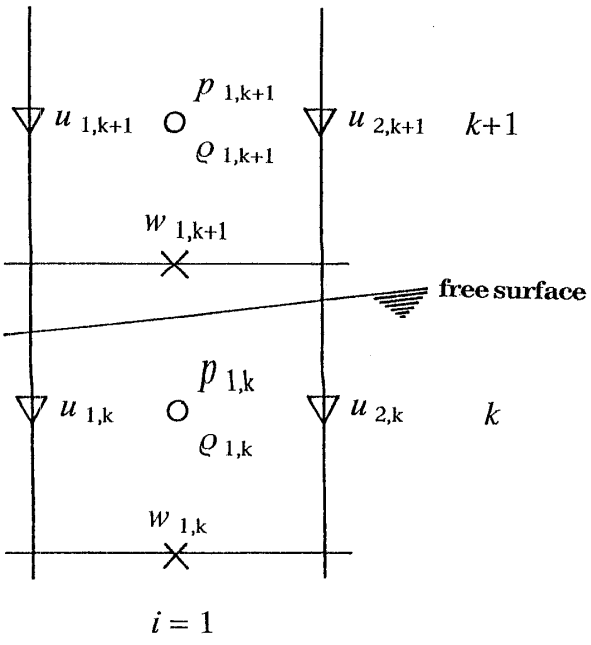

Fig. 9 Definition sketch for the wave making condition (case B).

where a is the half wave height, σ is the angular frequency, x is the wave number and D is the depth of the region, and (x, z) is the position of the velocity when the origin of the coordinate system is set at the first cell in the x-direction and the still water surface set at $z=0.0$. On the other hand, the inflow velocities in the region ⟨2⟩ are set at zero. The pressure in the cell is calculated by the Navier-Stokes equation as

$$p_1=\rho_1\frac{\Delta x}{\Delta t}(u_2-b_{x2})+p_2, \tag{44}$$

where b_{x2} is the sum of the right-hand-side of the x-directional Navier-Stokes equation except the pressure term.

The values of the marker-density are extrapolated with no-gradient in the horizontal direction.

4.5 Boundary conditions

At the top and bottom boundaries, the free-slip boundary condition is imposed on the velocity and the hydrostatic pressure is given since the vertical distances from the interface are sufficiently large in comparison with the wave height of interest. The absorbing outflow boundary condition is same with the case A, employing the added dissipation zone with the artificial damping scheme.

5. Simulated Waves by TUMMAC-VI Method

5.1 Condition of computation

The condition of computation is listed in Table 1. Except for the substantial difference it is set as same as the case A by the WISDAM-V method.

The grid spacing is variable in the vertical direction and the grids are clustered in the vicinity of the free-surface as shown in Fig. 10.

Being completely different from the case A, both the air region and the water region are computed simultaneously and the velocity vector field becomes as shown in Fig. 11. However, since the density of air is relatively very small, the action of air is not supposed to give influence on the water wave motion.

5.2 Effect of differencing scheme and time increment

The choice of the space-differencing scheme for the marker-density equation (29) is of significant impor-

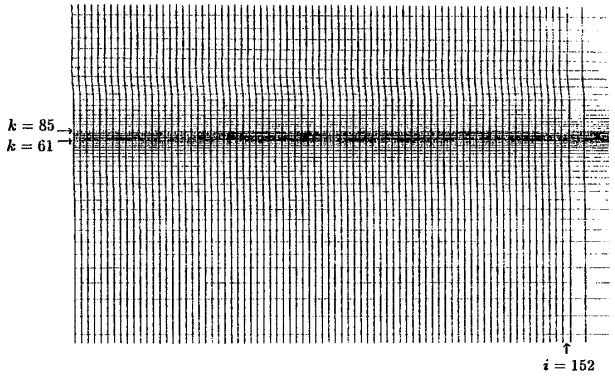

Fig. 10 Rectangular grid system.

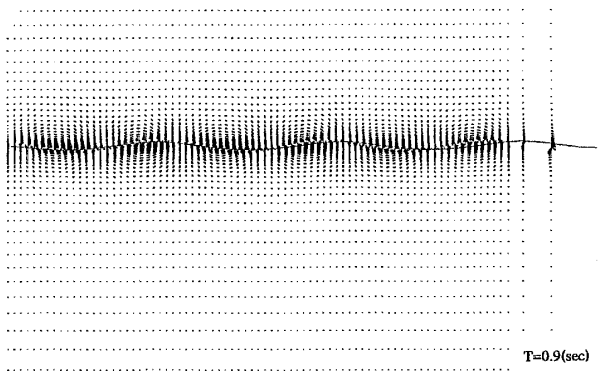

Fig. 11 Velocity vector field of the case B.

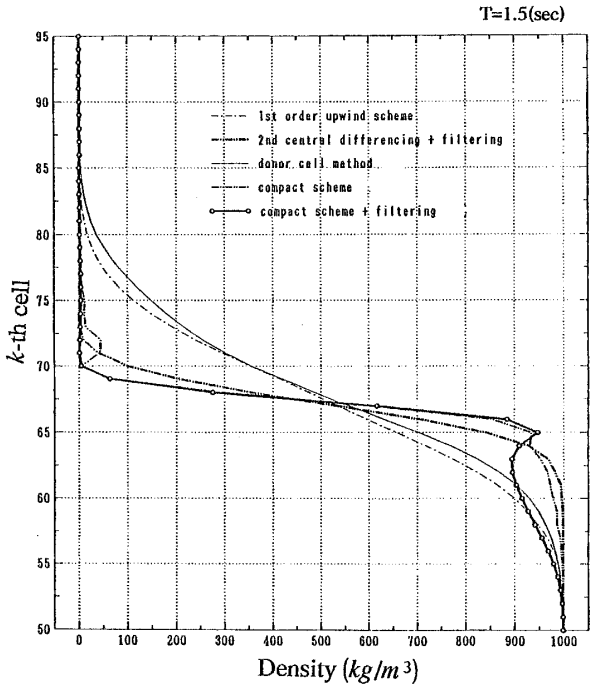

Fig. 12 Comparison of vertical variation of density at $t=1T$.

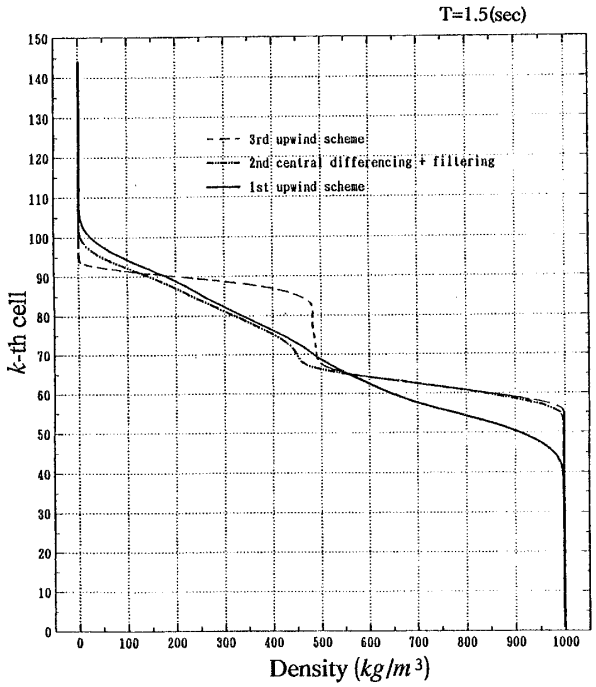

Fig. 13 Comparison of vertical variation of density at $t=10T$.

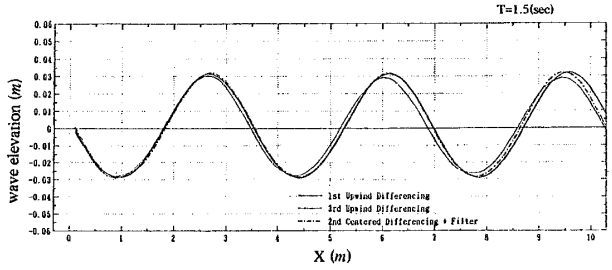

Fig. 14 Comparison of wave profiles at $t=10T$ by three differencing schemes.

tance.

For the accuracy of free-surface motion because the numerical error may dissipate it. The schemes described in section 4.3 are compared for one wave period of the case of $T=1.5$ sec, and the results are shown for the vertical variation of the marker-density in Fig. 12. It is obviously noted that the scheme which contains the error of the form of second derivative of velocity makes the marker-density diffused in the vertical direction, while others give rather steep variation of the marker-density. However, the compact scheme is lacking with robustness and has some difficulties in continuing wave generation for a number of wave period.

Three schemes are tested for ten wave periods and the results are shown in Fig. 13 in the same form and in Fig. 14 in the form of wave profiles. Since the interface moves up and down due to the wave motion, the marker-density is diffused by the elapse of time. It is hard to choose one from the three in Fig. 13, but from the standpoint of stability the third-order upwind scheme is used for the advanced examination.

It is noted that the value of time increment is a significant parameter on the degree of accuracy. As shown in Fig. 15 the discontinuous variation of the marker-density disappears and very steep slope is obtained when the time increment is set half of the previous case with the third-order upwind differencing scheme. Therefore, this scheme order upwind differencing scheme. Therefore, this scheme is employed with $\Delta t=1\times10^{-3}$ sec hereafter.

5.3 Results

The simulated waves for the three cases are presented in Figs. 16 to 18 in the same way with the case A. Since the wave profile used for comparison is one of the three

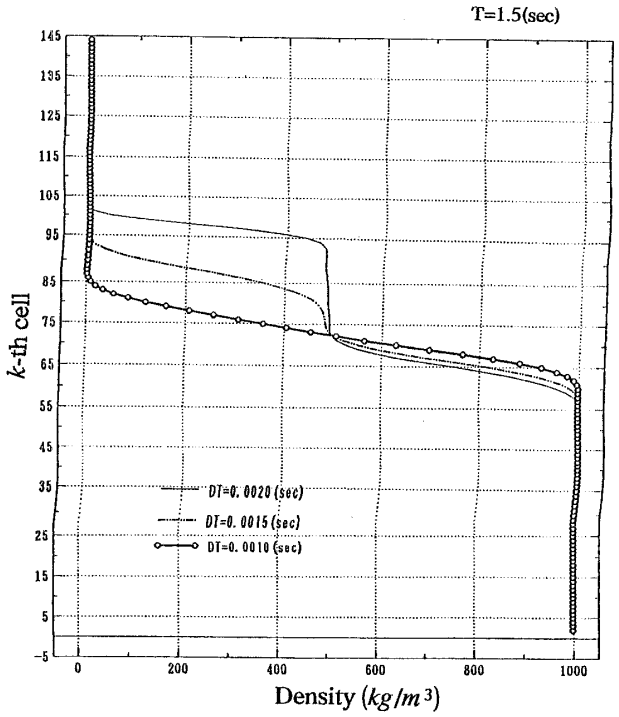

Fig. 15 Difference of vertical variation of density due to time increment.

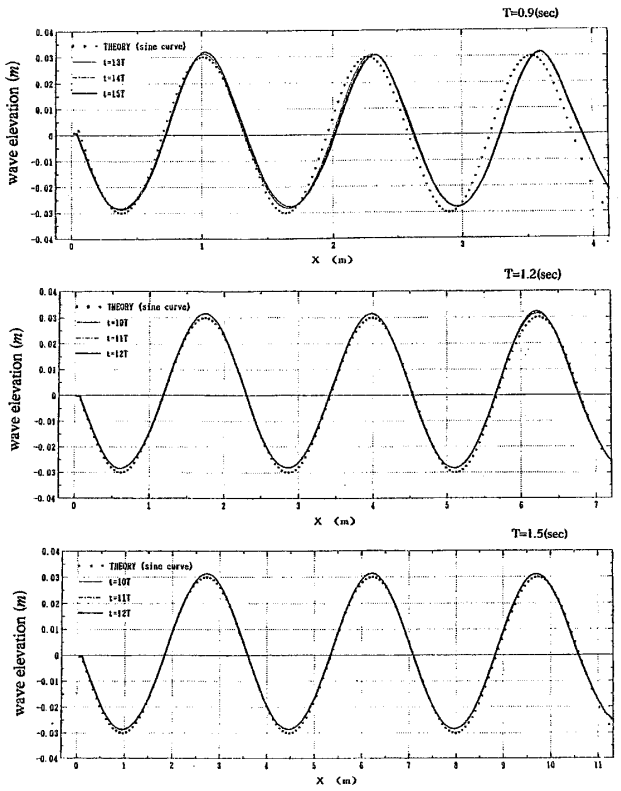

Fig. 16 Comparison of wave profile with a sine curve (case B).

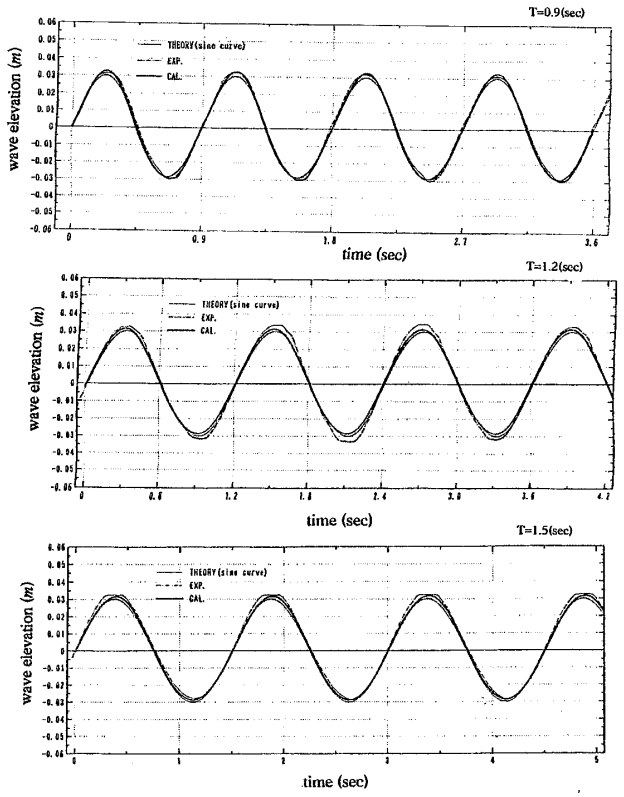

Fig. 17 Comparison of wave records with measurement (case B).

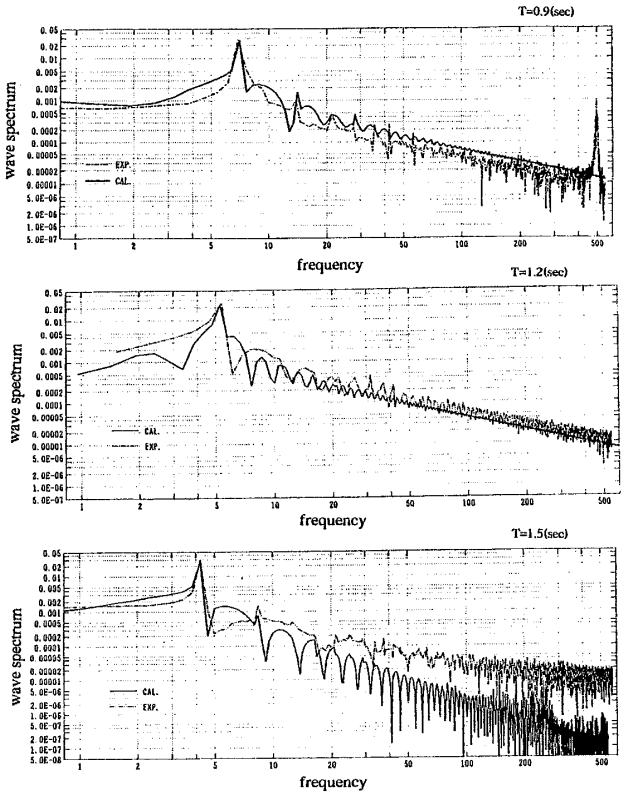

Fig. 18 Corparison of logarithmic wave spectrum (case B).

in Fig. 3 and it is different from the case A, the comparison shows some different features. However, the agreement is excellent considering the complicated treatments of the marker-density and related procedures. It is demonstrated that at least ten waves are generated with sufficient degree of accuracy and the error due to the numerical modeling is of the same order of magnitude with the physical experiment.

6. Conclusions

It is demonstrated that two numerical simulation methods can generate waves with sufficient degree of accuracy. This means that the numerical experiments can be performed with the numerical wave making apparatus with satisfactory accuracy. The hydrodynamic properties of ships and other floating structures will be tested both in the calm sea condition and in the heading wave condition by the same numerical method. Two methods have respective advantages and disadvantages. The WISDAM-V method can simulate delicate viscous motions on the body surface of gentle curvature, whereas the TUMMAC-VI method can simulate strongly interacting free-surface flow, such as 3D wave breaking. Both seem to be useful for a variety of problems.

Acknowledgment

The wave records of physical experiment were presented by Mr. S. Eguchi at the Prof. Fujino's laboratory which is highly appreciated. This research is partly supported by the Grant-in-Aid for Scientific Research of the Ministry of Education, Science and Culture.

References

1) Miyata, H., Nishimura, S. and Masuko, A.: Finite Difference Simulation of Nonlinear Waves Generated by Ships of Arbitrary Three-Dimensional Configuration, J. Computational Physics 60-3, 391-436 (1985).
2) Miyata, H.: Finite-Difference Simulation of Breaking Waves, J. Computational Physics 65-1, 179-214 (1986).
3) Sato, T., Miyata, H., Baba, N. and Kajitani, H.: Finite-Difference Simulation Method for Waves and Viscous Flows About a Ship, J. Soc. Nav. Archit. Jpn. 160, 14-20 (1986) (in Japanese).
4) Miyata, H., Sato, T. and Baba, N.: Difference Solution of a Viscous Flow with Free-Surface Wave About an Advancing Ship, J. Computational Physics 72-2, 393-421 (1987).
5) Watanabe, O., Zhu, M. and Miyata, H.: Numerical Simulation of a Viscous Flow with Free-Surface Wave About a Ship by a Finite-Volume Method, J. Soc. Nav. Archit. Jpn. 171, 507-519 (1992).
6) Miyata, H., Zhu, M. and Watanabe, O.: Numerical Study on a Viscous Flow with Free-Surface Waves About a Ship in Steady Straight Course by a Finite-Volume Method, J. Ship Research, Vol. 36, No. 4, 332-345 (1992).
7) Miyata, H., Katsumata, M., Lee, Y.G. and Kajitani, H.: A Finite-Difference Simulation Method for Strongly Interacting Two-Layer Flow, J. Soc. Nav. Archit. Jpn. 163, 1-16 (1988).
8) Park, J.C., Miyata, H., Tsuchiya, Y. and Kanai, M.: Wave-Wake Interactions About a Body of Revolution Advancing Beneath the Free Surface, Proc. 19th Symposium on Naval Hydrodynamics, Seoul, IV 1-18 (1992).
9) Rosenfeld, M. and Kwak, D.: Time-Dependent Solutions of Viscous Incompressible Flows in Moving Co-ordinates, Int. J. Num. Method in Fluid, Vol. 13, 1311-1328 (1991).
10) Yamazaki, R.: Expression of the Navier-Stokes Equations in General Coordinate Systems, J. West Japan Soc. of Nav. Archit., Vol. 75, 20-35 (1988) (in Japanese).
11) Hinatsu, M.: Numerical Simulation of Unsteady Viscous Nonlinear Waves Using Moving Grid System Fitted on a Free Surface, J. Kansai Soc. Nav. Archit. Jpn., No. 217, 1-12 (1992).
12) Inoue, M., Baba, N., Kitagawa, K. and Nakagawa, T.: Computation of Nonlinear Water Waves by Finite-Volume Method Using Free-Surface Fitted Coordinate System, J. Kansai Soc. Nav. Archit. Jpn., No. 217, 13-20 (1992).
13) Oranski, I.: A Simple Boundary Condition for Unbounded Hyperbolic Flows, J. Computational Physics 21, 251-269 (1976).
14) Wu, D.-M. and Wu, T.Y.: Three-Dimensional Nonlinear Long Waves Due to Moving Surface Pressure, Proc. 14th Symposium on Naval Hydrodynamics, Washington D.C., 103-129 (1982).
15) Chiba, S. and Kuwahara, K.: Numerical Analysis for Free Surface Flow around a Vertical Circular Cylinder, 3rd Symposium on Computational Fluid Dynamics, Tokyo, 295-298 (1989) (in Japanese).
16) Baker, G.R., Merion, D.I. and Orszag, S.A.: Applications of a Generalized Vortex Method to Nonlinear Free Surface Flows, 3rd International Conference on Ship Hydrodynamics, Paris, 179-192 (1981).
17) Romate, J.E.: Absorbing Boundary Conditions for Free Surface Waves, J. Computational Physics 99, 135-145 (1992).
18) Chan, R.K.C. and Street, R.L.: A Computer Study of Finite Amplitude Water Waves, J. Computational Physics 6, 68-94 (1970).
19) Hirsh, R.S.: Higher Order Accurate Difference Solutions of Fluid Mechanics Problems by a Compact Differencing Technique, J. Computational Physics 19, 90-109 (1975).
20) Baba, N. and Miyata: H., Higher-Order Accurate Difference Solutions of Vortex Generation from a Circular Cylinder in an Oscillatory Flow, J. Computational Physics 69-2, 362-396 (1987).
21) Sawada, K. and Takanashi S.: A Numerical Investigation on Wing/Nacelle Interference of USB Configuration, AIAA Paper 87-0455 (1987).
22) Kodama, Y.: Computation of Ship's Resistance Using an NS Solver with Global Conservation, J. Soc. Nav. Archit. Jpn. 172, 147-155 (1992).